Advanced materials analysis using synchrotron radiation and its application in engineering science

2004 J. Phys.: Condens. Matter 16 S3537

(http://iopscience.iop.org/0953-8984/16/33/014)

INSTITUTE OF PHYSICS PUBLISHING JOURNAL OF PHYSICS: CONDENSED MATTER

J. Phys.: Condens. Matter **16** (2004) S3537–S3548 PII: S0953-8984(04)80217-0

Advanced materials analysis using synchrotron radiation and its application in engineering science

Kiyoshi Iino and Norimasa Umesaki

Japan Synchrotron Radiation Research Institute (JASRI/SPring-8), 1-1-1 Kouto, Mikazuki-cho, Sayo-gun, Hyogo 679-5198, Japan

Received 6 May 2004
Published 6 August 2004
Online at stacks.iop.org/JPhysCM/16/S3537
doi:10.1088/0953-8984/16/33/014

Abstract

SPring-8 is one of the third-generation large synchrotron radiation facilities. The industrial application of synchrotron radiation carried out at SPring-8 has recently produced outstanding research results in the field of materials science. We have achieved the *in situ* observation of a galvannealing process for steel sheet, the structural analysis of amorphous thin SiO_x films, analysis of the precise crystal structure of a hydrogen storage alloy, x-ray imaging analyses of aluminium foam and snow-tyres and XAFS analysis of a catalyst for automobiles as examples of the industrial applications of synchrotron radiation.

1. Introduction

1.1. The industrial use of SPring-8

It is well known that synchrotron x-rays are a powerful tool for materials evaluation in industrial research and development. An increasing number of experimental projects have been undertaken recently by industrial users at SPring-8.

In order to promote the industrial use of SPring-8, a new industry support group was established at the Japan Synchrotron Radiation Research Institute (JASRI/SPring-8) in April 2001. The main function of this group is to provide a support service to industrial users that encompasses administration, acting as an interface between industrial users and SPring-8, consultancy work for industrial subjects, arranging meetings and training courses, technical and scientific support, management of the engineering science research beamline BL19B2 and collaboration with user companies. The BL19B2 beamline of the SPring-8 facility was constructed exclusively for industrial users. The purpose of this beamline is to promote the use of synchrotron radiation by industrial users. The beam usage and the number of application subjects have been significantly increased since 2001, when the industry support group started their activities.

In this paper, we will introduce the BL19B2 beamline and review some interesting experimental results from industrial projects that have been undertaken at SPring-8.

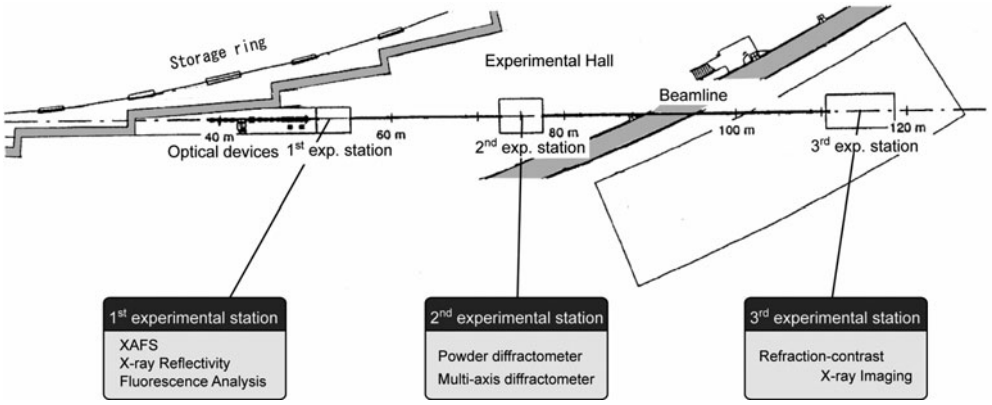

Figure 1. The layout of the engineering science research beamline (BL19B2) at SPring-8.

1.2. Engineering science beamline at SPring-8

SPring-8's design allows for a total of 62 beamlines, and there are currently 46 of these beamlines in operation. Each beamline is designed for a specific type of research. As we mentioned above, the engineering science research beamline (BL19B2) has been installed in SPring-8 to promote the use of synchrotron radiation by industrial users. The main techniques that are available on this beamline are x-ray absorption, diffraction, scattering and fluorescence analysis. The installation of BL19B2 began in 1999, and it was open for public use from September 2001.

The light source of BL19B2 is a bending magnet with a 0.679 T magnetic field, which provides x-rays with a critical energy of 28.9 keV. The horizontal divergence of the x-rays is limited to 1.4 mrad by a fixed mask. A standard double-crystal monochromator is placed at a distance of 42.5 m from the light source. The adjustable, inclined geometry of the monochromator enables the use of photon energies between 5 and 117 keV by selecting the Si(111), (311) and (511) diffraction planes. Two mirror supports for the 1 m long mirror substrate are located in tandem at 47.9 and 49.5 m from the source. SiO_2 mirror substrates coated with platinum are used. These are used to reject the higher harmonics of incident x-rays and/or for focusing the x-rays by bending the mirror in the meridional direction.

This beamline has three experimental stations situated along its length (figure 1). The first experimental station is located at 51 m from the light source and consists of spectrometers for XAFS measurement, x-ray reflectivity measurement and fluorescence analysis. The second station is located at 77 m from the light source and contains a powder diffractometer and a multi-axis diffractometer. The final station is located at 111 m from the light source and consists of equipment for refraction-contrast x-ray image experiments.

The XAFS spectrometer enables x-ray absorption measurements in transmission mode, fluorescence mode and conversion electron yield mode. Three lengths of ionization chamber (i.e. 65, 170 and 310 mm) were prepared for transmission mode measurements. The current in the ionization chamber is amplified to a voltage, converted to frequency and then counted. Four different gases, i.e., helium, nitrogen, argon and krypton (and their gas mixtures), can be injected. For the fluorescence mode, a Lytle-type detector, a germanium single-element solid-state detector (Ge SSD) and a silicon drift-chamber detector (SDD) can be used. The Lytle-type detector contains an aluminium solar slit and a 50 mm long ionization chamber. The element of the Ge SSD has an effective area of 200 mm^2 and a thickness of 10 mm,

enabling it to detect more than 95% of the incident x-rays. The element of the SDD has an effective area of 5 mm^2 and a thickness of 0.3 mm. The SDD can be operated without liquid nitrogen. The research areas that require this XAFS station include the following examples: the characterization of thin films of capacitor materials and gate insulator materials for ULSI and magnetic devices, local structural analysis of catalysts for automotive engine exhaust gases and electrode material for rechargeable lithium-ion batteries.

To perform accurate structural analysis by powder diffraction studies, a Debye–Scherrer camera is installed at the second experimental station. This camera, which has a radius of 286.5 mm, has an image plate (IP) on the 2θ arm as a detector. The pixel size of the IP can be selected between 50 and 100 μm. The high energy beam with its high flux allows us to collect a large number of Bragg reflections with high counting statistics from a small amount of powdered specimen. Because high energy x-rays are used, it is not necessary to take into consideration the effects of absorption, even for materials involving heavy elements such as rare-earth metals. This will make it possible to measure high quality powder diffraction data for crystalline materials.

The second experimental station also includes a Huber multi-axis diffractometer. It is composed of a conventional four-circle goniometer (φ, χ, ω, θ) with four additional axes (ωz, θz, ωa, $2\theta a$). The diffractometer is controlled by SPEC and GUI programs. This diffractometer can be tuned for residual stress measurement and structural analysis of thin films, surfaces and interfaces. A Eulerian cradle with a gap within the χ circle is adopted to cover a wide scattering angle from $-45°$ to $160°$ (without a blind region) for the measurement of residual stress. Precise linear X, Y and Z stages (60 mm $\times$ 60 mm $\times$ 25 mm) on the φ axis enable us to observe the three-dimensional residual stress profiles of bulky samples. It is expected that residual stress in the inner region of bulky samples could be observed by using high energy x-rays. Making the blades of the slits from Ta can help to eliminate high energy x-rays at less than 100 keV. The ωa and $2\theta a$ axes are equipped to use an analyser crystal. The two additional axes (ωz and $2\theta z$) are very useful for controlling the glancing angle and the take-off angle of x-rays at the sample surface. The in-plane crystallographic structure of a thin film can be easily observed by glancing incidence x-ray scattering. CTR and x-ray reflectometry are also available.

The third experimental station includes a system for refraction-contrast imaging examinations. This includes an x-ray camera which has a 5 mm $\times$ 5 mm field of view and about 10 μm minimum resolution.

2. Results of experiments carried at the engineering science beamline (BL19B2)

2.1. Diffraction techniques

2.1.1. In situ observation of a galvannealing process for steel sheet. Galvannealed steel sheets are widely used in the automotive industry to protect car bodies from corrosion. In the industrial process of galvannealing steel sheets, steel substrates are dipped into molten zinc containing a small amount of aluminium, then annealed in a furnace at about 500 °C. Since the coating of the galvannealed steel sheets mainly consists of Fe–Zn intermetallic compounds such as $FeZn_7$ (δ_1 phase) and $FeZn_{13}$ (ζ phase), it is very important to be able to study the growth behaviour of those compounds during a galvannealing process in order to understand the roughness or the mechanical properties of the coating after the process. However, because these reactions occur in a short period (up to 60 s) it is very difficult to detect them by static analyses using a specimen quenched after annealing, such as cross-sectional observation of the coating with an electron microscope or measurement of the iron content of the coating.

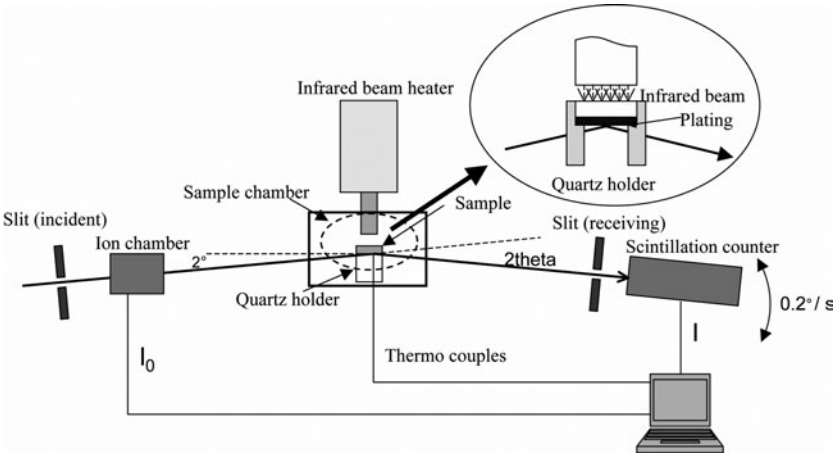

Figure 2. A schematic illustration of the *in situ* observation system for thermal treatment of galvannealing steel sheet.

Therefore, a rapid detection system is required to observe those reactions dynamically, i.e., by '*in situ* observation'. In order to perform *in situ* observations, the penetration depth of the x-rays and the time definition of the detector are important factors, since it is necessary to observe the whole of the coating (10–20 μm thickness) and to monitor a reaction that is completed within 60 s. An easy method of achieving good time definition for the detector is to increase the source intensity. Therefore, high energy and high intensity synchrotron radiation is suitable for the *in situ* observation.

The schematic illustration of the *in situ* observation system incorporated in beamline BL19B2 is shown in figure 2. A galvanized steel sheet sample was mounted on a quartz holder in a sample chamber filled with N_2 gas, and was heated from the polished side with an infrared beam heater mounted on the multi-axis goniometer. Taniyama *et al* [1] obtained heating-time-dependent diffraction peak profiles with either a scintillation counter or an image plate. When the scintillation counter was used, the peak profiles were measured at intervals of 5 s, while being scanned at an angular velocity of 0.2° s^{-1}. When the imaging plate was used, the peak profiles were measured every second. Figures 3(a) and (b) show diffraction peak profiles obtained with a scintillation counter and an image plate, respectively. The samples had zinc coatings containing small amounts of aluminium. The start of the heating time shown in the figures was taken as the point when the coating fully melted. An increase in the diffraction peak intensity, identified as $\delta_1(330)$, was successfully observed in the profiles. The diffraction peak could not be observed in the profiles shown in figure 3(a), which were gathered up to 20 s after the coating melted, and therefore it was considered that the 30 μm coating was too thick to allow the detection of the diffraction peaks of the δ_1 phase growing near the interface between the coating and the steel substrate at the beginning of the annealing process. On the other hand, the diffraction peak could not be observed up to 7 s after the coating melted in figure 3(b). In this measurement, the thickness of the coating does not affect the observation of the diffraction peaks of the δ_1 phase growing near the interface (as mentioned above) because the diffraction peak of the steel substrate was clearly obtained. It is well known that aluminium in the coating forms an Al-rich layer between the coating and the steel substrate, retarding the growth of Fe–Zn intermetallic compounds [2]. Therefore, the variation in the peak profiles indicates that the Al-rich layer prevents the growth of δ_1 phase at the beginning of the annealing

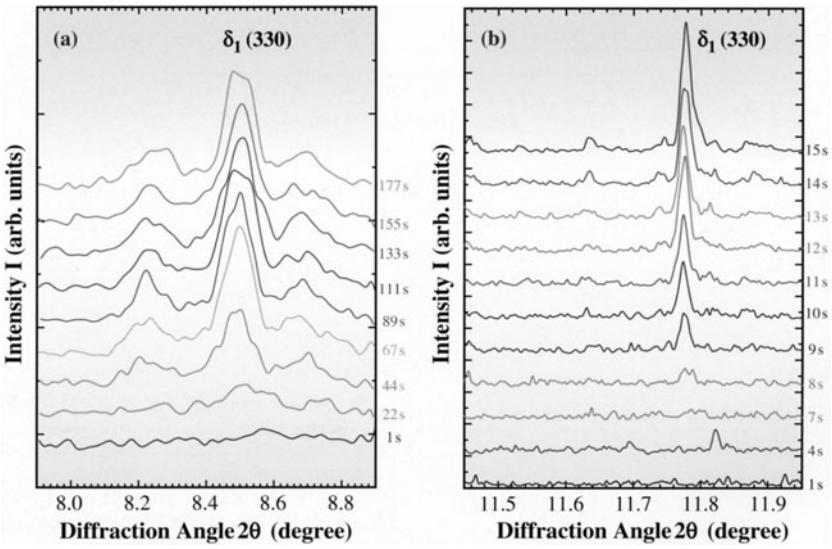

Figure 3. Diffraction profiles obtained from galvanized steel sheet during annealing. (a) Wavelength of incident x-rays: 0.0319 nm, thickness of the coating: 30 μm, detector: scintillation counter. (b) Wavelength of incident x-rays: 0.0443 nm, thickness of the coating: 10 μm, detector: image plate.

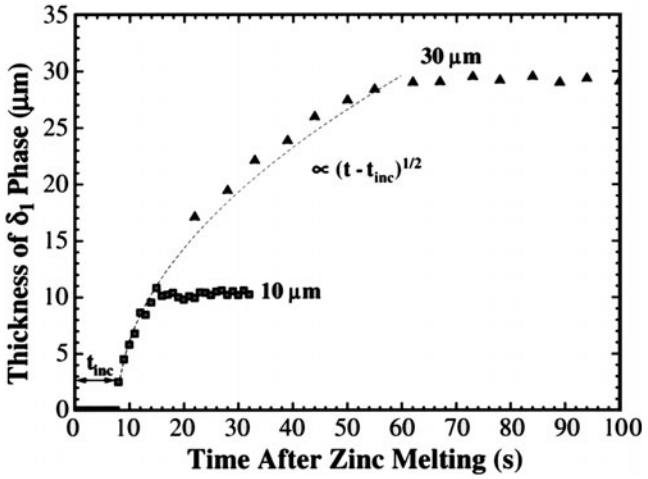

Figure 4. The relationship between estimated thickness of the δ_1 phase and annealing time.

process. The period from the beginning of annealing to the beginning of Fe–Zn intermetallic compound growth is known as the 'incubation period'. The time dependence of the thickness was estimated (as shown in figure 4) by assuming that the δ_1 phase grows in a layer-by-layer manner. The estimated thickness of the δ_1 phase increased following the parabolic law with annealing time, taking into account the incubation period (t_{inc}). These results suggest that the growth of the δ_1 phase is dominated by the diffusion of Fe atoms and Zn atoms in the coating. This result could be useful for improving the manufacturing process for high quality galvannealed steel sheets.

2.1.2. Grazing incidence x-ray diffraction of amorphous thin films. Amorphous thin films are widely used in microelectronics and optical devices, such as the amorphous silicon oxide films used as gate insulators in VLSI and the anti-reflection coating film of optical components. These amorphous films are very thin. In the case where a silicon oxide film is used as a gate insulator, the film thickness is less than 10 nm. Characterization of these amorphous films is essential in order to develop and fabricate suitable amorphous films, since the structures of these amorphous films would have a significant effect on their electronic and optical characteristics.

Grazing incidence x-ray scattering is a suitable technique for investigating thin film structures and surface structures. In grazing incidence x-ray scattering, the incident x-rays impinge on the sample surface with a very small angle of incidence. Generally, the dielectric constant or the refractive index of condensed matter is less than one in the x-ray region, and there is a critical angle of incidence for the total reflection of x-rays. In the condition where the incident angle is smaller than the critical angle of the substrate, the penetration of the x-rays is limited to some tens of nanometres from the sample surface and the background noise originating from the x-rays scattered from the substrate can be reduced.

Hirosawa *et al* [3] applied grazing incidence x-ray scattering to investigate the structure of amorphous silicon oxide films for anti-reflection coatings. A sample of SiO_x anti-reflection coating film was prepared on a Si(001) substrate by ECR plasma sputtering. The density and thickness of the deposited films were determined to be 2.125 g cm^{-3} and 58.2 nm by x-ray reflection analysis. Bulk amorphous silica (fused silica) was also observed in the transmission geometry (Laue case) as a reference. The mass density of the fused silica was 2.20 g cm^{-3}. Grazing incidence x-ray scattering experiments were performed using the multi-axis diffractometer in BL19B2 in SPring-8. The sample was mounted in a chamber filled with He gas to reduce background scattering due to air. The energy of the incident beam was selected to be 8.0 keV and the incident angle was set at 0.16°. The critical angle of the SiO_x film was estimated to be 0.21° at 8.0 keV from its mass density, so the penetration depth of the x-rays was estimated to be 10 nm. Thus, the observed intensity in this experiment should mainly be derived from the deposited SiO_x film.

The observed intensity decreased sharply between scattering angles of 6° and 9°, as shown in figure 5. The profiles at less than 8° mainly consist of the background due to air scattering, since almost the same profile was observed without the sample (blank). The background observed without the sample in the low scattering angle region could be fitted well by the formula

$$A \exp(-B\theta)$$

where A and B are optimized parameters and θ is half of the scattering angle. Thus, in the correction procedure used to derive the interference function, the background for the small scattering angles is subtracted from the observed data using the function described above. The optimized parameters A and B are determined by fitting with the observed profile between 6° and 8°. The estimated background is indicated by the thin dotted curve in figure 5.

The interference function, defined as $i(q) = \alpha I(q) - \Sigma f_i^2$, is shown in figure 6(a). In this expression, $I(q)$ is the geometrically corrected and background-subtracted observed intensity, while α is the normalization factor. The form factors of Si and O are described by f_i. The normalization factor α is determined to minimize the sum of the squares of $I(q)$. There are two positive peaks at 21 and 37 nm^{-1} in the interference function of the deposited SiO_x film (solid curve in figure 6(a)). The amplitudes of these positive peaks are nearly the same. On the other hand, the interference function of the bulk amorphous silica has an intense peak at 15.7 nm^{-1} and some weak peaks around 40–50 nm^{-1} (dotted curve in figure 6(a)). The large difference

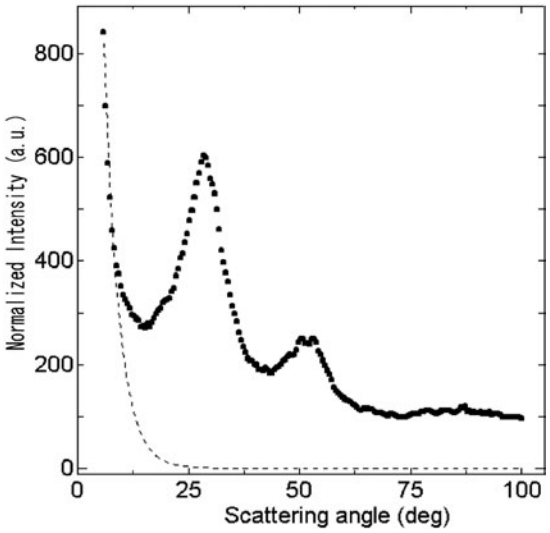

Figure 5. The x-ray diffraction profile of the deposited amorphous SiO_x thin film. The dotted thin curve shows the estimated background.

of the interference functions of the SiO_x film and the bulk amorphous silica indicates that the deposited SiO_x film has a structure different from that of the bulk amorphous silica.

The radial distribution function of the deposited SiO_x film is derived by the Fourier transformation of $qi(q)/\Sigma f_i^2$ in the range 5.0–62 nm^{-1}, as shown in figure 6(b) (solid circle). The radial distribution function of the bulk silica glass is shown by the open circles in the same figure. The thin dotted curves shown simultaneously in the same figure are the averaged electron densities of the SiO_x film and the bulk amorphous silica estimated from their mass densities. The peaks at 0.168 nm (A), 0.242 nm (B), 0.304 nm (C) and 0.412 nm (D) for the bulk amorphous silica correspond to the pair correlations of the Si–O, O–O, Si–Si and Si–O second shells [4]. On the other hand, the radial distribution function of the deposited SiO_x film is very different. The pair correlation of Si–O is unclear in the radial distribution function of the SiO_x film. Instead of the pair correlations of Si–O, the radial distribution function of the SiO_x film has peaks at 0.235 and 0.388 nm. As for the silicon crystal, the interatomic distances of the first- and second-nearest neighbours are 0.235 and 0.384 nm. However, there is no indication of the pair correlations of the third- and fourth-nearest neighbours in the silicon crystal in the radial distribution function of the deposited SiO_x film. This suggests that the deposited SiO_x film is composed of tetrahedra formed by silicon, and that the silicon atoms in the film are partially oxidized rather than completely oxidized.

2.1.3. Hydrogen storage alloy. Hydrogen is considered to be one of leading candidate clean energy sources. Therefore, the development of safe storage for hydrogen becomes a key technology. So-called hydrogen storage alloys have suitable properties for the safe and efficient storage of hydrogen, so they have been studied for some time now. Magnesium is considered to be one of the most promising materials for reversible hydrogen storage, due to its low density and high storage capacity. In order to develop a high performance hydrogen storage system with this material, it is essential to understand the nature of the bonding of magnesium atoms and hydrogen atoms in the crystal. Noritake *et al* [5] made precise powder diffraction measurements and subsequently analysed the charge density distribution in MgH_2 using the

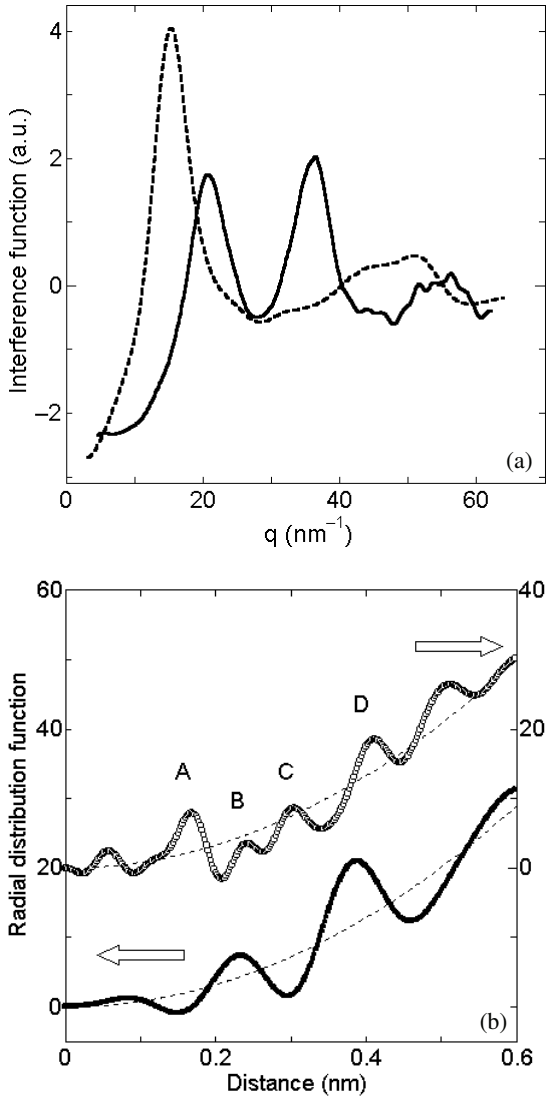

Figure 6. (a) The interference function of the deposited amorphous SiO_x thin film (solid curve) and bulk silica glass (dotted curve). (b) Radial distribution function curves of the deposited amorphous SiO_x thin film (solid circle) and the bulk silica glass (open circle).

MEM (maximum entropy method)/Rietveld method. Charge density is typically investigated by means of x-ray diffraction, but the diffraction intensity from hydrogen atoms is very weak. So far, analysing the hydrogen in metal hydrides by means of x-ray diffraction has proved to be difficult. In SPring-8, high brilliance synchrotron radiation x-rays yield outstanding quality diffraction patterns and allow us to precisely determine the position of hydrogen atoms in the lattice (figure 7(a)).

The MEM is a method of finding the most probable value from experimental data by the maximization of entropy, and is based on information theory [6, 7]. The charge density of MgH_2 was analysed by the MEM/Rietveld method using the measurement data (figure 7(b)). The results show weak covalent bonds between Mg and H, as well as between H and H. The

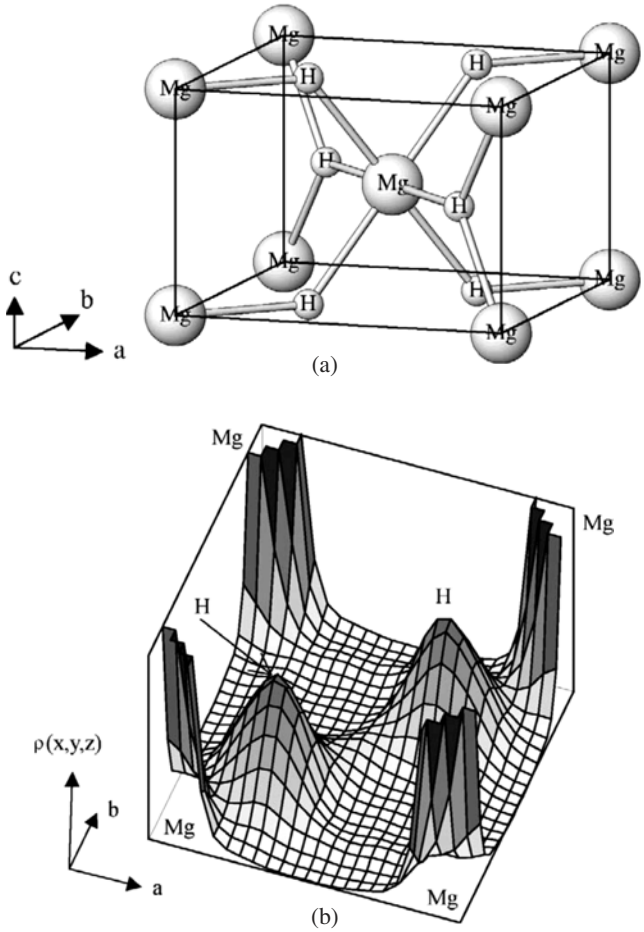

Figure 7. (a) The crystal structure of MgH_2 (rutile); (b) the charge density distribution function in the (001) plane of MgH_2.

charge density in the interstitial region is extremely low, which precludes the existence of metallic bonding. From the estimation of the number of electrons within a sphere around the Mg and the H atoms, the ionic charge in MgH_2 was denoted as $Mg^{1.91+}H^{0.26-}$. It was concluded that the ionic bonding between Mg and H atoms must be made weaker in order to improve the dehydrogenation performance of MgH_2.

2.2. Imaging techniques

2.2.1. Compression behaviour of foam aluminium. In recent years, it has become increasingly important to reduce the weight of automobiles due to energy and environmental considerations. Moreover, the increasing use of aluminium in automobiles is expected to improve human safety. Foam aluminium has desirable features such as lightness, a high modulus of rigidity and high 'crashworthiness' (shock resistance). In particular, foam aluminium has several excellent properties for both reducing vehicle weight and for improving human safety in crash situations. However, a suitable technology for evaluating the mechanical properties of foam aluminium has not yet been established.

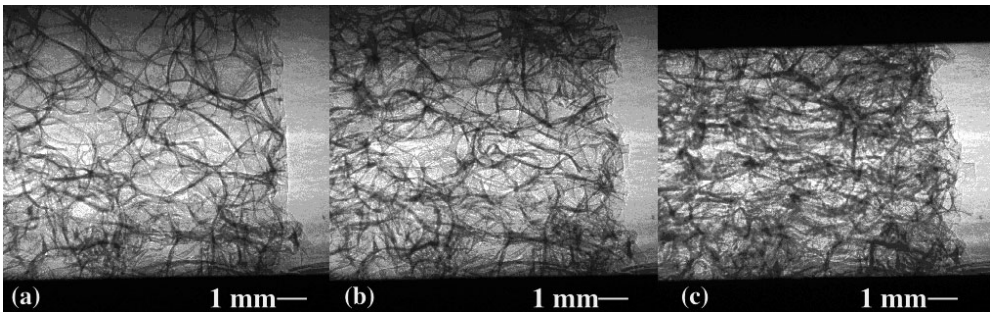

Figure 8. Three scenes from an *in situ* image of a foam aluminium compression test.

Watanabe *et al* [8] carried out an *in situ* examination of the compression behaviour of foam aluminium by using refraction-contrast imaging. They succeeded in taking *in situ* pictures of the porous structure when it was compressed, and they clarified how the porous structure influenced the pressure–displacement curve. The refraction-contrast images were taken at 2 s intervals while the sample was compressed by a compression-testing machine at a rate of 1 mm/1s. X-rays with an energy of 33 keV were used for this application, while an x-ray CCD camera with a 1280 × 1024 pixel area and a 6.7 μm pixel size was used as the detector.

Figures 8(a)–(c) shows three *in situ* images when the sample was compressed. Through careful analysis of the series of images, it was observed that there were two modes of destruction that affected the foam: buckling destruction and explosion destruction. This research is expected to lead to the establishment of a basic structural design protocol for automotive material using foam aluminium and some improvement of its crushability properties.

2.2.2. New snow-tyres for use on ice. A new material for use in high performance tyres was invented recently, consisting of a compound of rubber including dispersed glass fibres. It is believed that the dispersed glass fibres protrude from the surface of the rubber and work as a series of small studs. Kishimoto *et al* [9] carried out *in situ* observation of the behaviour at the contact between the newly developed rubber and ice. Figure 9 shows a series of refraction-contrast images that were taken during a sequence of movements, as follows: (1) Press the rubber against the ice. (2) Slide the pressed rubber on the ice. (3) Lift the rubber from the ice. The glass fibres stuck into the ice when the rubber was pressed against the ice (figure 9(b)). As the rubber slid across the ice, the glass fibres scratched the surface of the ice (figure 9(c)). The glass fibres did not break when the rubber was finally lifted from the surface (figure 9(d)). Through these observations, they proved that this material is highly effective on ice and guarantees the performance of tyres made from this material on winter roads.

2.3. XAFS techniques

2.3.1. Catalysts for automobiles. Nagai *et al* [10, 11] investigated the relationship between oxygen storage/release capacity (OSC) and the atomic-level structure of CeO_2–ZrO_2 mixed oxides by XAFS. The OSC is one of the most important functions required of automobile three-way catalysts (TWCs) in order to efficiently remove harmful compounds such as hydrocarbons, CO and NO_x from automotive exhaust gases. It has recently been discovered that the mixed oxides of ZrO_2 and CeO_2 show good OSC and thermal stability. Furthermore, it is possible to improve the OSC of CeO_2–ZrO_2 via modifications in the preparation methods. Because CeO_2–ZrO_2 has been widely utilized for commercial catalysts, it was desirable to clarify the relationship between the OSC and the structure of CeO_2–ZrO_2.

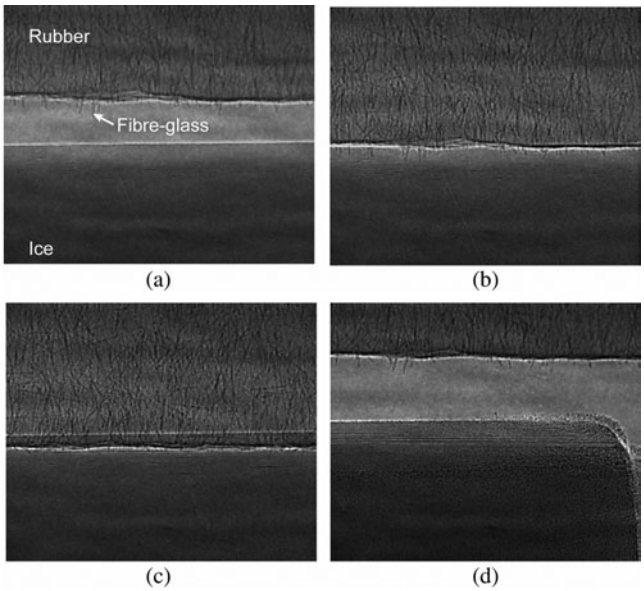

Figure 9. Refraction-contrast imaging of the contact between glass-fibre impregnated rubber and ice. (a) Before compression; (b) the moment of contact; (c) the rubber slipping on the ice; (d) the rubber lifted up from the ice.

The Ce K edge (40.5 keV) and the Zr K edge (18.0 keV) EXAFS of the samples were examined. CeO_2–ZrO_2 samples with the same composition ratio (Ce/Zr = 1) were prepared by the following methods:

(1) CZ55-1 was prepared by a precipitation process using CeO_2 powder and zirconyl nitrate solution.
(2) CZ55-2 was prepared by a co-precipitation process using cerium nitrate and zirconyl nitrate solutions.
(3) CZ55-3 was synthesized by heating CZ55-2 at 1473 K under reductive conditions.

The OSC of the samples at 773 K were observed to be, in order, CZ55-1 (0.08 mmol-O_2/g) < CZ55-2(0.44 mmol-O_2/g) < CZ55-3(0.75 mmol-O_2/g). Consequently, CZ55-3 exhibited the highest OSC.

Throughout the quantitative EXAFS curve-fitting analysis, the difference in the atomic-level structure for each sample was revealed. CZ55-1 consists of pure CeO_2 and ZrO_2. Ce-rich and Zr-rich domains still remain in CZ55-2. A $Ce_{0.5}Zr_{0.5}O_2$ solid solution forms homogeneously in CZ55-3 at the atomic level (figure 10). As mentioned above, the OSC values of the samples were in the order CZ55-1 < CZ55-2 < CZ55-3. It can be seen that the OSC increases with enhanced homogeneity of the CeO_2–ZrO_2 solid solution at the atomic level. Through this research, it is clear that catalyst design at the atomic level is necessary to develop high performance catalysts for practical use.

3. Conclusion

We introduced some results of the industrial application of the synchrotron radiation of SPring-8. In fact, we can say that these results show the successful use by individual private companies

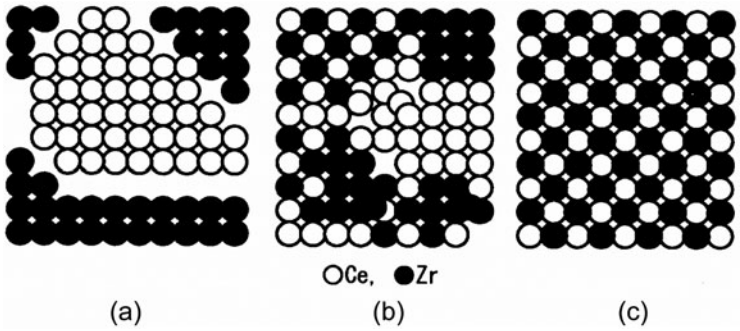

Figure 10. A model illustration of the cation–cation network for the CeO_2–ZrO_2 samples with the same chemical composition ($Ce/Zr = 1$). CZ55-1 consists of pure CeO_2 and ZrO_2. Ce-rich and Zr-rich domains still remain in CZ55-2. $Ce_{0.5}Zr_{0.5}O_2$ solid solution in CZ55-3 forms homogeneously at the atomic level.

of the facilities at SPring-8. To produce more ground-breaking results, research collaborations, such as university–company joint ventures, should be promoted more and clear research strategies for the development of new materials should be planned.

References

[1] Taniyama A, Takayama T, Arai M, Kawata H, Sato M, Hirosawa I, Fukuda T and Mizuki J 2002 *Proc. Int. Conf. on Designing of Interfacial Structures in Advanced Materials and their Joints* p 385
[2] Bablik H 1950 *Galvanizing (Hot Dip)* 3rd edn (London: Spon Ltd) p 204
[3] Hirosawa I, Uehara Y, Sato M and Umesaki N 2004 *J. Ceram. Soc. Japan* **112** S1476
[4] Poulsen H F, Neuefeind J, Neumann H B, Schneider J R and Zeidler M D 1995 *J. Non-Cryst. Solids* **188** 63
[5] Noritake T, Aoki M, Towata S, Seno Y, Hirose Y, Nishibori E, Takata M and Sakata M 2002 *Appl. Phys. Lett.* **81** 2008
Noritake T, Towata S, Aoki M, Seno Y, Hirose Y, Nishibori E, Takata M and Sakata M 2004 *J. Alloys Compounds* **356–357** 84
[6] Takata M, Nishibori E and Sakata M 2001 *Z. Kristallogr.* **216** 71
[7] Takata M, Umeda B, Nishibori E, Sakata M, Saito Y, Ohno M and Shinohara H 1995 *Nature* **377** 46
[8] Watanabe T, Ariga Y, Miyoshi T and Makii K 2003 *Adv. X-ray Chem. Anal. Japan* **34** 187 (in Japanese)
[9] Kishimoto H 2002 *Polym. Preprints Japan* **51** 2118 (in Japanese)
[10] Nagai Y, Yamamoto T, Tanaka T, Yoshida S, Nonaka T, Okamoto T, Suda A and Sugiura M 2001 *J. Synchrotron Radiat.* **8** 616
[11] Nagai Y, Yamamoto T, Tanaka T, Yoshida S, Nonaka T, Okamoto T, Suda A and Sugiura M 2002 *Catal. Today* **74** 225